Int. J. Heat Mass Transfer. Vol. 36, No. 2, pp. 371–381, 1993
Printed in Great Britain

0017–9310/93 $6.00 + 0.00

Effects of angle of attack on mass transfer from a square cylinder and its base plate

S. Y. YOO,† R. J. GOLDSTEIN‡ and M. K. CHUNG§

† Department of Mechanical Design Engineering, Chungnam National University, Daejeon, Korea
‡ Department of Mechanical Engineering, University of Minnesota, Minneapolis, MN 55455, U.S.A.
§ Department of Mechanical Engineering, Korea Advanced Institute of Science and Technology, Daejeon, Korea

(*Received* 17 *December* 1990 *and in final form* 17 *April* 1992)

Abstract—A naphthalene sublimation technique is employed to investigate the convective mass transfer process from a square cylinder and its base plate in a flow of air. Distributions of local mass transfer coefficients on each face of the cylinder change dramatically with the angle of attack. The average Sherwood number has a minimum value at $\alpha = 12$–$13°$, and a maximum value at $\alpha = 20$–$25°$ where α is the angle of attack. A comparison of the present mass transfer measurement with earlier heat transfer measurements, using the heat/mass transfer analogy, shows good agreement at average transfer rates, but notable differences in local values, especially near the reattachment point. A remarkable enhancement of mass transfer due to the horseshoe vortex system is observed on the square cylinder and on the base plate near the plate–cylinder junction. As the angle of attack increases, the mass transfer peak created by counterrotating vortices diminishes. On the other hand, the influence of the corner vortex remains strong regardless of the angle of attack. Surface flow on the base plate is visualized using the oil–lampblack technique. Streaks of the corner vortex and the counterrotating vortices in the visualization picture compare well with the trails of the peak of mass transfer created by these vortices.

INTRODUCTION

THE SQUARE cylinder is an important bluff body in connection with long-standing questions about the heat/mass transfer mechanisms in separated and reattached flow regions. The flow approaching a square cylinder in a two-dimensional region stagnates and accelerates on the front face, separates and reattaches on the side face, and sheds vortices from the rear face. The effects of such complex flow conditions on the heat/mass transfer mechanism vary with the angle of attack, α. The flow patterns can be classified into three regimes according to the angle of attack [1]. For $\alpha < 13°$, a shear layer separated at the leading edge does not reattach onto the side face (perfect separation regime). The flow reattaches to the side face for $14° < \alpha < 35°$ (reattachment regime). For $35° < \alpha < 45°$, the flow field resembles one about a wedge (wedge flow regime). Igarashi [2, 3] measured local and average heat transfer from a square prism at various angles of attack using thermocouples. The average heat transfer was obtained at a constant wall temperature condition, and the local heat transfer coefficient was measured under the condition of a constant heat flux. In the present study, local mass transfer rates on a square cylinder in a two-dimensional region are measured with different angles of attack, and they are compared with Igarashi's [2] heat transfer data.

Mass transfer rates on a square cylinder and its base plate in the three-dimensional flow region near the base of the cylinder are also measured. A horseshoe vortex system is the dominant flow phenomenon in the plate–obstacle junction region. In a previous paper [4], the present authors reported the effects of multiple vortices formed around a square cylinder mounted vertically on a base plate for $\alpha = 0°$ on the mass transfer. A primary horseshoe vortex, a corner vortex, a pair of counterrotating vortices on the cylinder, and another pair of counterrotating vortices on the base plate were found to enhance mass transfer dramatically. Variation of their effects with the angle of attack will be described in the present paper. A naphthalene sublimation technique is employed which is adaptable to the precise measurement of local transfer rates in regions with a large gradient of transport.

Flow visualizations are performed separately from the mass transfer experiments. An oil–lampblack technique is used to visualize the surface flow on the base plate at various angles of attack. The response of the horseshoe vortex system to the variation of the angle of attack is investigated by comparing the surface flow visualization patterns with the measured mass transfer distribution.

EXPERIMENTAL APPARATUS AND PROCEDURE

The experimental apparatus is devised to measure the local rate of naphthalene loss due to sublimation from the four faces of a square cylinder and also from the base plate when they are exposed to an air flow. The apparatus includes a wind tunnel, test cylinders and plate, and an automated sublimation depth

NOMENCLATURE

d	side length of square cylinder, 25.4 mm in the present study	U_∞	free stream velocity
D	mass diffusion coefficient of naphthalene vapor in air	x	streamwise distance measured from the center of cylinder base
h_m	mass transfer coefficient	y	distance along the cylinder axis measured from the base
n	exponent in the heat/mass transfer analogy equation, 1/3 in the present study	z	spanwise distance measured from the center of cylinder base.
Nu	Nusselt number	Greek symbols	
p	circumferential distance measured from the front-left edge of cylinder in counterclockwise direction	α	angle of attack, angle between free stream velocity and side wall
Pr	Prandtl number	Δt	net sublimation depth of naphthalene in the wind tunnel
Pr_t	turbulent Prandtl number	$\Delta\tau$	total exposure time in the wind tunnel
Re_d	Reynolds number, $U_\infty d/\nu$	ν	kinematic viscosity of air
Sc	Schmidt number, ν/D	ρ_s	density of solid naphthalene
Sc_t	turbulent Schmidt number	$\rho_{v,w}$	naphthalene vapor density on the surface.
Sh	Sherwood number, $h_m d/D$		

measurement system. Only an outline of the experimental apparatus and procedure are given in this section; full details are described by Yoo [5].

An open-circuit, suction-type wind tunnel is used. It has a rectangular test section 610 mm wide, 305 mm high, and 2500 mm long. Air speeds of 8.7–17.9 m s^{-1} are used, and the corresponding Re_d, the Reynolds number based on the length of a side of the square cylinder, is 13 600–28 000. The freestream turbulence intensity is less than 0.6% over the entire range of speeds. Test cylinders and mounting plates are shown in Fig. 1. The test cylinder used for the two-dimensional measurements has a side length of 25.4 mm (1 in.) and height of 305 mm (12 in.), and is machined with 1 mm deep and 76.2 mm long section in the outer middle surface to hold the naphthalene casting. A derlin plate used for two-dimensional measurements has the same configuration as the hole of the tunnel's bottom wall, and has a marker to indicate the angle of attack. The cylinder used for three-dimensional measurements is machined with a 1 mm deep and 101.6 mm long section to hold naphthalene. The base plate has a 152.4 mm × 182.9 mm × 1.5 mm deep naphthalene active region, and has the same configuration as the derlin plate of the two-dimensional measurements. The cylinder is inserted into a removable

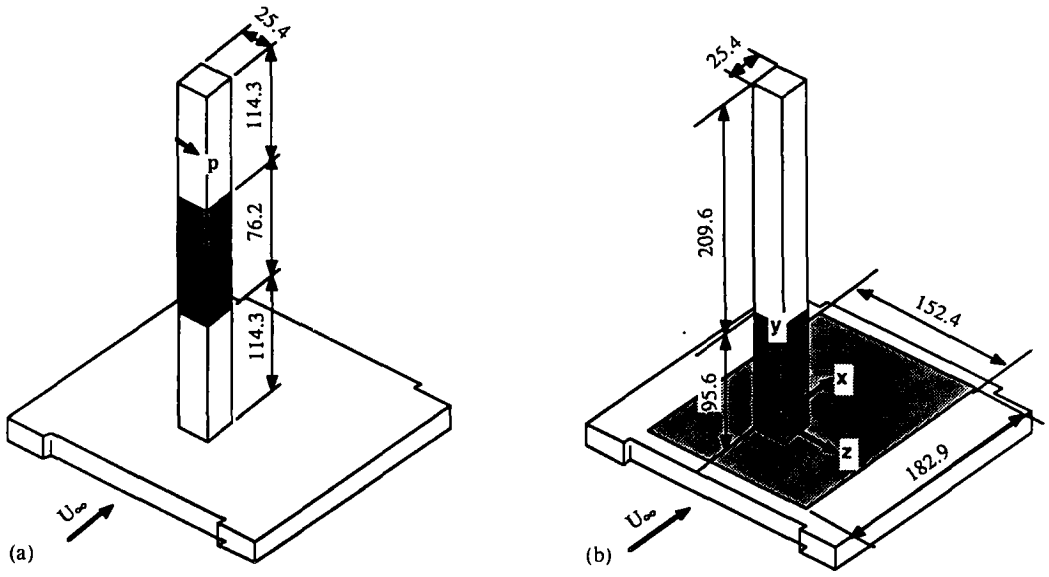

FIG. 1. Sketch of test cylinder mounted on the base plate: (a) for measurements in two-dimensional flow region; (b) for measurements in plate–cylinder junction region.

adapter of the base plate so that the naphthalene covered portion extends from 6 mm below the upper surface of the plate to 95.6 mm above it. The adapter is designed to rotate for measurements with various angles of attack. The automated sublimation depth measurement system consists of a depth gage along with a signal conditioner, a digital multimeter, two stepper-motor driven positioners, a hardware unit for motor control, and two sets of personal computer, HP-85 and IBM/AT.

The mass transfer coefficient can be determined from

$$h_m = \rho_s \Delta t / \rho_{v,w} \Delta \tau \quad (1)$$

where ρ_s is the density of the solid naphthalene, $\rho_{v,w}$ is the naphthalene vapor density on the surface, Δt is the net sublimation depth, and $\Delta \tau$ is the total exposure time in the wind tunnel. Total naphthalene sublimation depth is calculated from the change in measured surface elevations before and after the exposure, and the excess sublimation due to the natural convection during the sublimation depth measurement period is subtracted from the total sublimation. The sublimation depth was generally 0.05–0.20 mm in the two-dimensional flow region, and 0.05–0.45 mm in the three-dimensional flow region. The empirical equation of Ambrose *et al.* [6] is used to determine the naphthalene vapor pressure. From the ideal gas law, naphthalene vapor density on the surface is then evaluated. The results are expressed in terms of the Sherwood number

$$Sh = h_m d / D \quad (2)$$

where d is the side length of the square cylinder. The mass diffusion coefficient of naphthalene in air, D, is determined from Mack's measurement data and the correlation of Chen and Othmer [7] which accounts for temperature and pressure variations. Chen [8] has reviewed correlations for naphthalene vapor pressure and diffusion coefficient, and has recommended the Ambrose equation and Mack's measurement data, respectively. Uncertainty analysis according to Kline and McClintock [9] reveals that the estimated errors of the Sherwood numbers are within 6% in the entire range of our measurements.

RESULTS AND DISCUSSION

Local mass transfer on a square cylinder in the two-dimensional region was measured at various angles of attack, and compared with earlier heat transfer measurements to examine the heat/mass transfer analogy. Mass transfer distributions both on the square cylinder and on the base plate around the plate–cylinder junction region were obtained at various angles of attack. Surface flow visualization patterns on the base plate were compared with the measured mass transfer distribution.

Two-dimensional region

Distributions of local Sherwood number at various angles of attack are shown in Fig. 2. For $\alpha < 13°$ (separation regime—Fig. 2(a)), little effect of α on Sh is seen on the front face 0–1. However, Sherwood

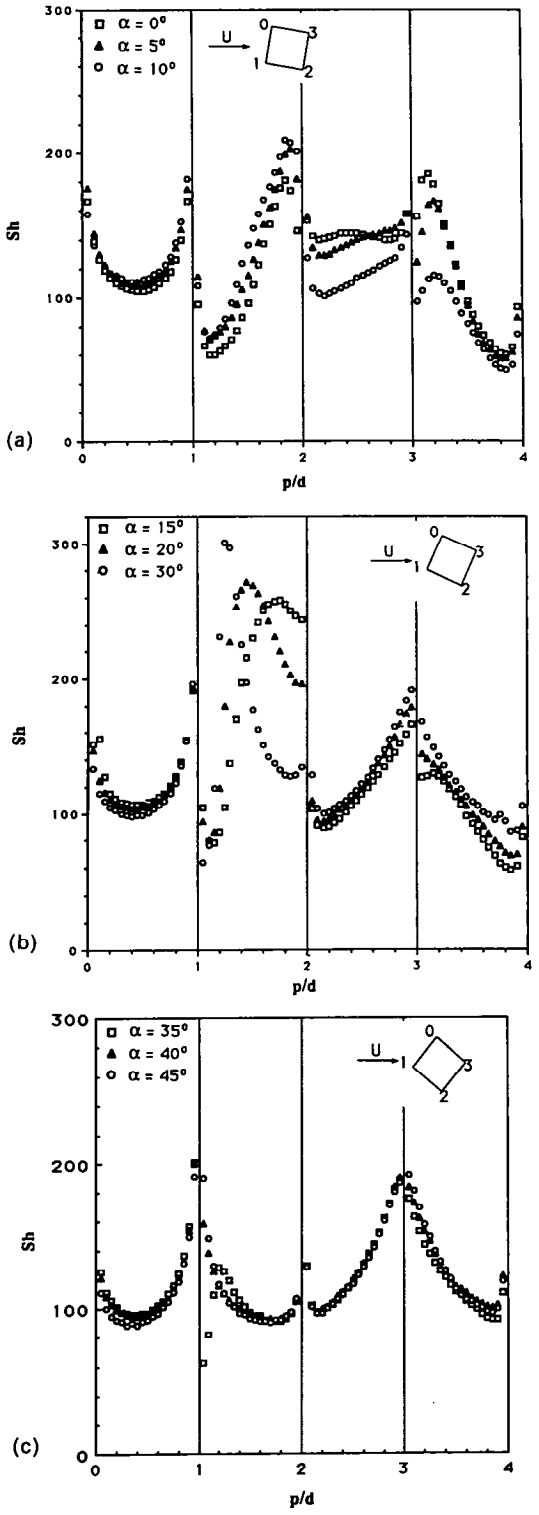

FIG. 2. Distribution of local Sherwood number at various angles of attack: (a) $\alpha = 0$, 5 and 10°; (b) $\alpha = 15$, 20 and 30°; (c) $\alpha = 35$, 40 and 45°.

numbers on side faces 1–2 and 3–0, and on the rear face 2–3 decrease considerably with an increase in α. This causes a reduction of the average mass transfer rate with α in this flow regime. For $13° < \alpha < 35°$ (reattachment regime—Fig. 2(b)), the Sherwood number on the side face 1–2 increases significantly owing to the reattachment of the separated shear layer. The maximum value of Sh increases and the location of the maximum moves toward the leading edge 1 with an increase in α. Little effect of α on Sh is found on the other faces, and a local maximum is noticed at the rear stagnation point 3. Beyond $\alpha = 35°$ (wedge flow regime—Fig. 2(c)), distributions of the local Sherwood number are almost the same over the whole surface regardless of α, and the variation of Sh is similar to that seen on a circular cylinder.

Figure 3 presents a comparison of the present mass transfer measurements with heat transfer data of Igarashi [2]. His data were recalculated using the heat/mass transfer analogy relation

$$Sh/Nu = (Sc/Pr)^n \tag{3}$$

where the exponent n is taken to be 1/3, as was used by Igarashi [2] for correlation of his data. For $\alpha = 0°$, general trends of the heat and mass transfer variation are very similar to each other, Fig. 3(a). It is apparent that the slopes of the mass transfer variation on the front and side faces are steeper than those found with heat transfer. This implies that mass transfer may be more sensitive to flow change than heat transfer, or the heat transfer results may be affected by wall conduction. On the rear face, the mass transfer shows much lower convective transport than the heat transfer. Figure 3(b) shows a comparison with heat transfer measurements at an angle of attack of 20°. The trends are similar, but differences are found on the side face 1–2 where the separated shear layer reattaches. It is commonly assumed that the position of the maximum heat transfer coefficient is essentially in agreement with that of the time-averaged reattachment point [10]. There are some reports [11] in which the position of the maximum heat transfer is located somewhat upstream of the reattachment point. Meanwhile the position of the maximum mass transfer coefficient in the present study is found far upstream, and maximum value is much higher than that of heat transfer. One might infer that the mass transfer mechanism is somewhat different from that of heat transfer near the reattachment point. The heat and mass transfer mechanisms in the separated and reattached flows are governed by the turbulent Prandtl number and turbulent Schmidt number, respectively, rather than laminar ones from which the analogy relation, equation (3), is derived. Simpson and Field [12] computed the turbulent Schmidt number in a boundary layer on a flat plate using the mass transfer coefficient and velocity and concentration profile data of Kendall [13], and compared that to their turbulent Prandtl number measurement. Their results showed that Pr_t and Sc_t are not likely to be the same even in simple flow patterns. You *et al.* [14] measured and compared the Stanton number and skin friction coefficients on convexly curved turbulent boundary layers. The turbulent Prandtl number played an important role in the relationship between the skin friction coefficient and Stanton number, which represent momentum transfer and heat transfer, respectively. Unfortunately, there are not sufficient data for Pr_t and Sc_t to study their effect on the heat/mass transfer analogy.

Nevertheless, good agreement is found in the average transfer rates, as shown in Fig. 4, which indicates that the simple analogy relation is still applicable in an average sense. The present average values are obtained from the summation of local values. Both Igarashi and the present results are much higher than those of Hilpert [15]. Figure 5 shows the variation of the average mass transfer with the angle of attack. Up to an angle of $\alpha = 12°$, the average Sherwood num-

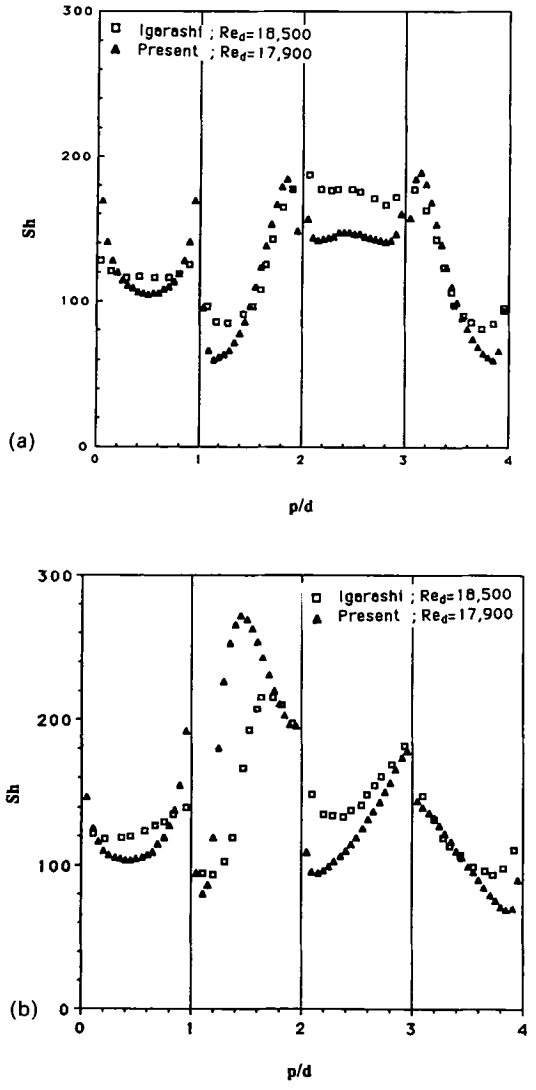

FIG. 3. Comparison of local mass transfer rate with heat transfer measurement using the heat/mass transfer analogy: (a) $\alpha = 0°$; (b) $\alpha = 20°$.

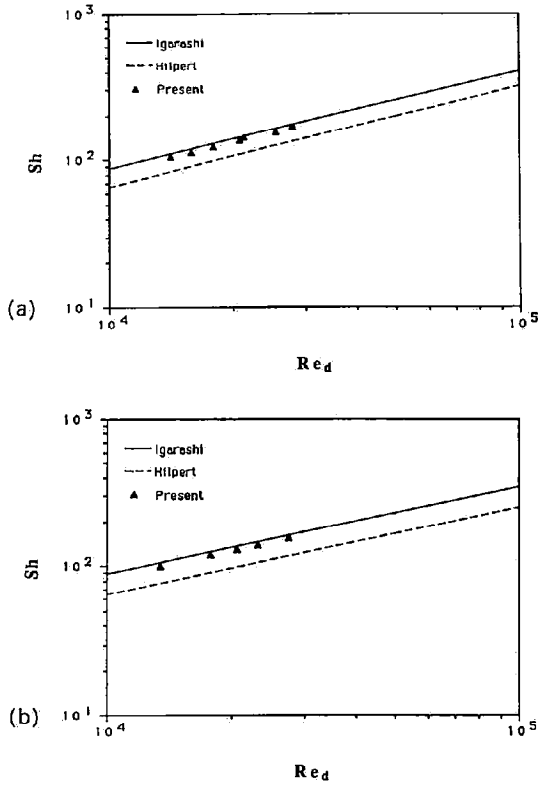

FIG. 4. Comparison of average mass transfer rate with heat transfer measurement using the heat/mass transfer analogy: (a) $\alpha = 0°$; (b) $\alpha = 45°$.

ber decreases with increasing α. Beyond $\alpha = 13°$ the value increases due to reattachment of the separated shear layer, then at $\alpha = 20$–$25°$ the value reaches a maximum, and above 25° it decreases gradually with increasing α. The mass transfer process is closely connected with the characteristics of the flow. A comparison of the average transfer rates at various angles

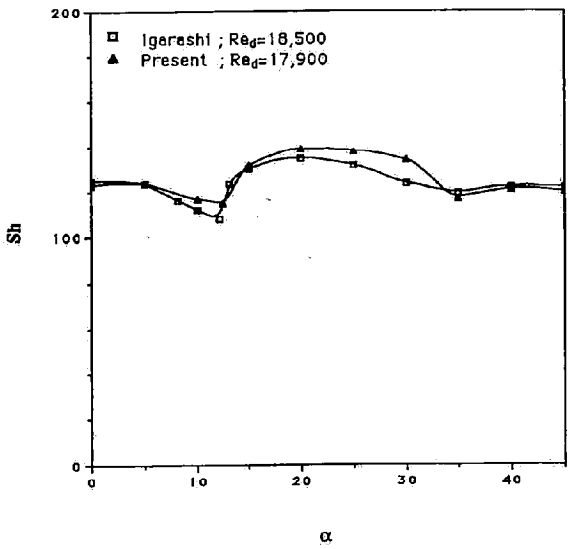

FIG. 5. Comparison of variation of average mass and heat transfer rate under different angles of attack using the heat/mass transfer analogy.

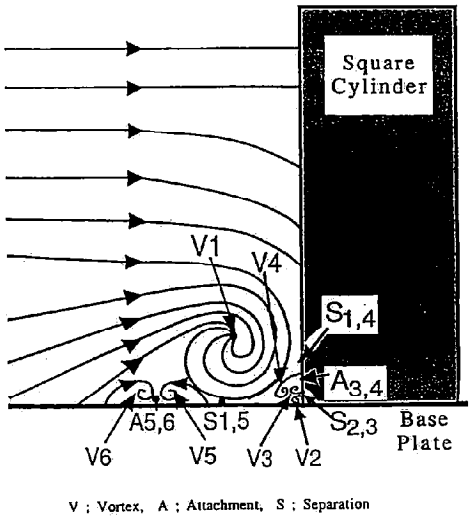

FIG. 6. Schematic of the assumed horseshoe vortex system in the x–y plane.

of attack is also presented in Fig. 5. For $\alpha < 13°$ and $\alpha > 35°$, good agreement of both results is seen, but somewhat higher values are observed for the mass transfer when the separated flow reattaches on the side face 1–2.

Plate–cylinder junction region

A boundary layer flow approaching an obstacle mounted vertically on a flat plate undergoes three-dimensional separation, and the separated boundary layer rolls up to establish a horseshoe vortex system. As many as six vortices, cf. Fig. 6, were inferred from the mass transfer [4]. Figure 7 shows contours of the Sherwood number on each face of the square cylinder for $\alpha = 0°$. Three peaks on the front face are produced by the corner vortex V2 ($y/d \approx 0.02$), a pair of counterrotating vortices V3 and V4 ($y/d \approx 0.08$) and the primary horseshoe vortex V1 ($y/d \approx 0.3$–0.5). The corner vortex V2 moves down to the base plate on the front face, and enhances mass transfer almost three times the two-dimensional value at the front edge. It moves away from the base plate when it passes by the side face. On the rear face, the Sherwood number increases from zero at the base and approaches gradually to the two-dimensional value. The region affected by the base plate extends to a height, y, of about one side length of the cylinder.

Contours of the Sherwood number on the base plate for different angles of attack are shown in Fig. 8, and variation of Sherwood numbers on the base plate along the centerline is presented in Fig. 9. For all of the tests, the Reynolds number is approximately 18 800 and the displacement thickness at the location of the cylinder is about 2.475 mm. As can be seen from the figure, the vortex dramatically augments the mass transfer. The corner vortex V2 formed at the plate–cylinder interface causes a locally high transport

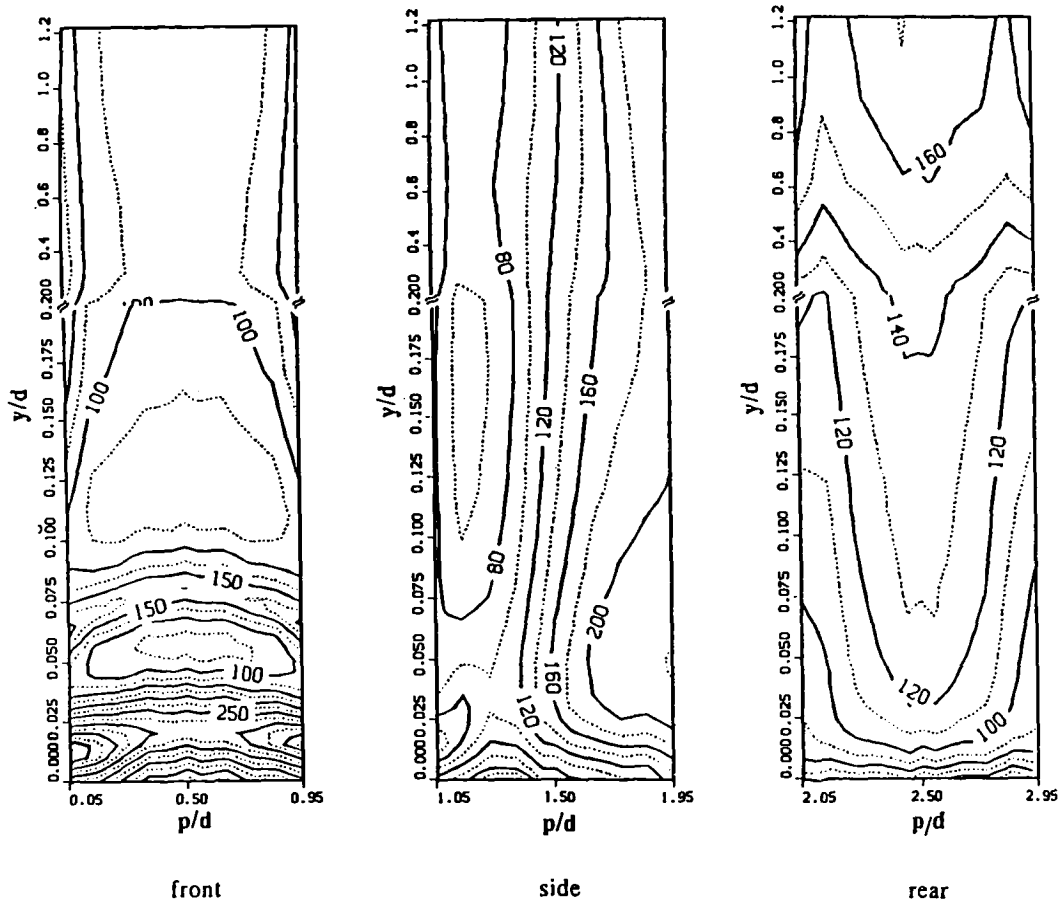

FIG. 7. Contours of the Sherwood number on the square cylinder ($\alpha = 0^\circ$, $Re_d = 18\,800$).

region near the front edge of the cylinder. With separation, it moves away from the side face, and eventually touches the trailing edge of the side face. It finally disappears when it interacts with the recirculating flow behind the cylinder, where it produces another local maximum. Mass transfer augmentation due to the corner vortex (V2) and the counterrotating vortices (V5 and V6) decrease rapidly. This is not because the strength of the vortex is weakened, but because it moves away from the base plate as seen on the side face of the cylinder. This also can be explained from the fact that longitudinal vortices embedded in the boundary layer usually maintain their coherence over a long streamwise distance [16]. As the angle of attack increases, the mass transfer peak created by the counterrotating vortices (V5 and V6) diminishes, and almost disappears at $\alpha = 45^\circ$, which is very similar to what occurs on the base near a circular cylinder [17]. On the other hand, the influence of the corner vortex (V2) on the mass transfer enhancement remains strong regardless of the angle of attack. Reattachment of the separated shear layer is seen on the lower side face of the cylinder at $\alpha = 20^\circ$. Contours of Fig. 8 clearly show the trail of the peaks created by the counterrotating vortices and corner vortex. The whole affected area on the base plate extends approximately $1.5d$ upstream, $1.5d$ to the side, and $3d$ downstream from the center of the cylinder location.

Surface flow visualization

The oil–lampblack visualization patterns of the surface flow on the base plate at various angles of attack are shown in Fig. 10. In a low speed zone or separated flow region the mixture remains stationary, giving rise to a black area in the visualized pattern. On the contrary, a white region implies active fluid motion (high shear). The narrow white line created by the corner vortex starts at the front face of the cylinder, turns at the edge and passes by the side face. It finally goes into the separated boundary layer, and disappears in the rear wake region of the cylinder while interacting with the reattached flow. The wide black zone upstream of the white line is a low velocity pocket situated between the corner vortex V2 and the primary horseshoe vortex V1. Beyond this black zone is a large region populated with horseshoe-like streaks with open ends downstream. Forward of the cylinder, these streaks represent a backflow, as is consistent with the direction of rotation of the vortex V1. These regions are swept around the sides of the cylinder. On the

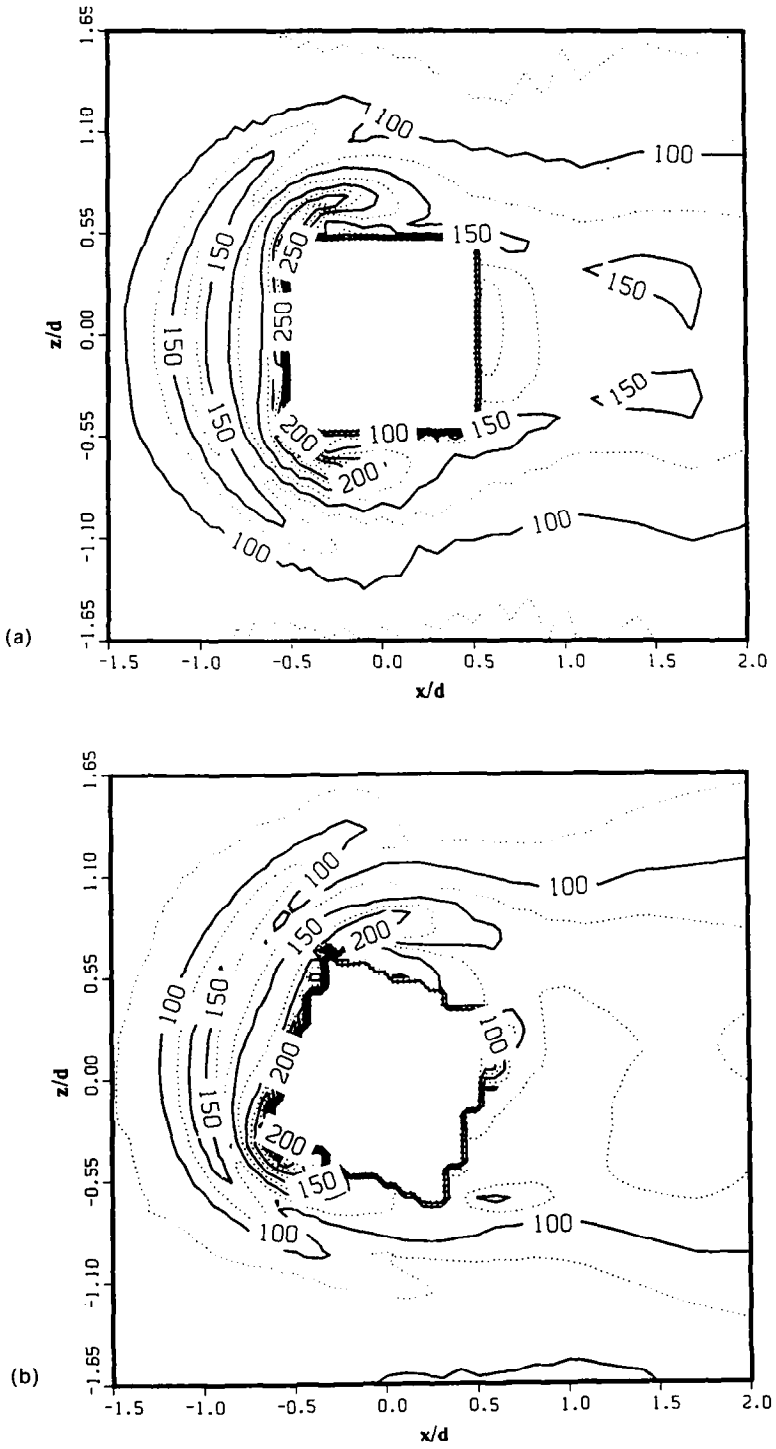

FIG. 8. Contours of the Sherwood number on the base plate ($Re_d = 18\,800$): (a) $\alpha = 0°$; (b) $\alpha = 20°$; (c) $\alpha = 45°$.

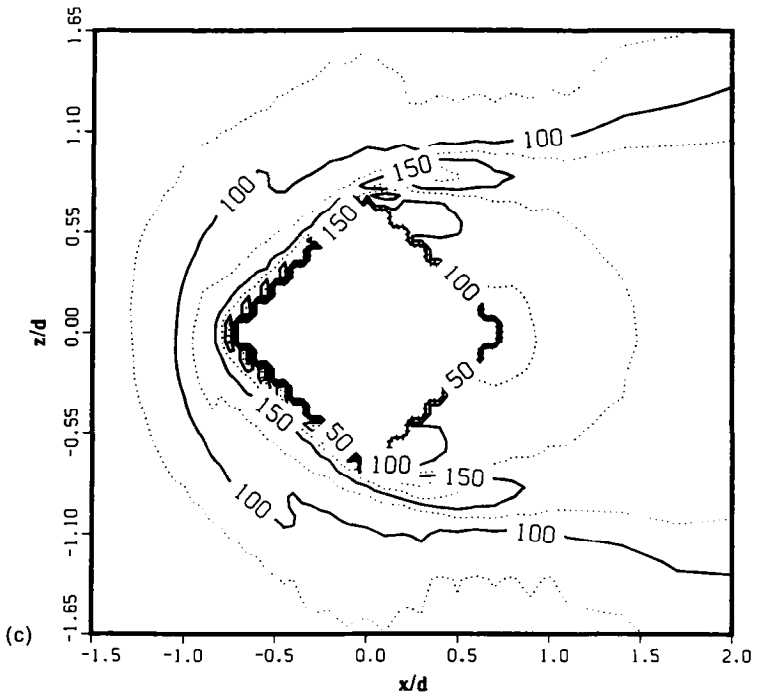

FIG. 8.—*Continued.*

forward edge of this zone, another distinct white line is seen, which depicts the presence of vigorous fluid motion. Until this present study, this region was considered as a part of the streak of the primary horseshoe vortex [18]. A comparison with the trace of the peaks of mass transfer, as shown in Fig. 8, shows that this line is apparently created by the pair of the counterrotating vortices V5 and V6. The region directly downstream of the cylinder appears black in the visualization picture, which is the wake behind the cylinder. This zone is followed by the backflow region, which is apparently connected with the reattached flow.

White streaks in the visualization picture due to the corner vortex and the pair of counterrotating vortices compare quite well, respectively, with the trails of the peak of the Sherwood number created by these vortices in the contour plot shown in Fig. 8. Another interesting feature for $\alpha = 20°$ is that the corner vortex emerges into the separated boundary layer before the separated flow reattaches to the side face of the cylinder.

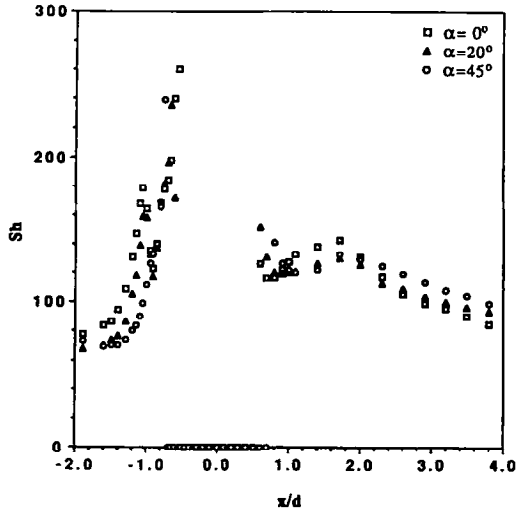

FIG. 9. Variation of the Sherwood number on the base plate along the centerline ($Re_d = 18\,800$).

CONCLUSIONS

Detailed measurements of the mass transfer both on the square cylinder and its base plate at various angles of attack were performed using a naphthalene sublimation technique. A summary of major results is as follows:

(1) Distribution of local mass transfer coefficients on each face of the square cylinder in the two-dimensional region changes dramatically with the angle of attack, and these variations are closely connected with the flow regime. The average Sherwood number has a minimum value at $\alpha = 12$–$13°$ and has maximum at $\alpha = 20$–$25°$.

(2) Average values of heat and mass transfer are in good agreement with each other, but local rates of mass transfer are much higher than those of heat transfer when the separated flow reattaches to the side face.

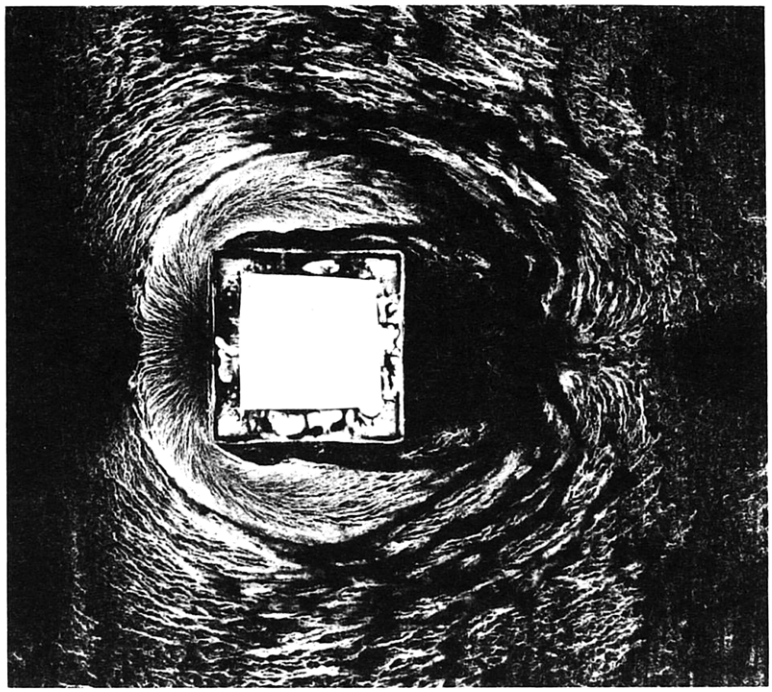

(a)

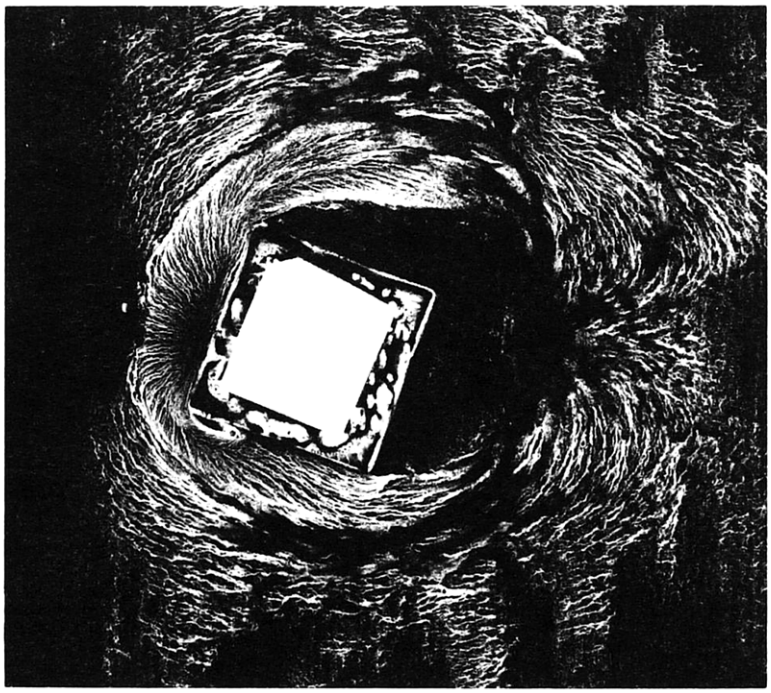

(b)

FIG. 10. Visualization of the surface flow on the base plate ($Re_d = 28\,800$): (a) $\alpha = 0°$; (b) $\alpha = 20°$; (c) $\alpha = 45°$.

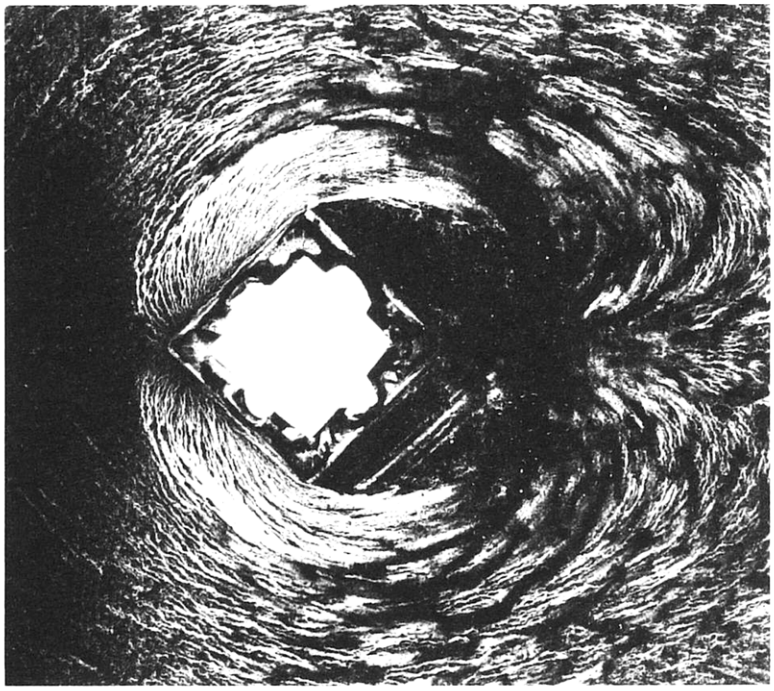

(c)

FIG. 10.—*Continued.*

(3) Multiple vortices, which include the primary horseshoe vortex, the corner vortex and two pairs of counterrotating vortices, affect the mass transfer process in the vicinity of the plate–cylinder junction. The influenced region on the cylinder extends to a height of about one side length of the cylinder, and the whole affected area on the base plate extends approximately $1.5d$ upstream, $1.5d$ to the side, and $3d$ downstream from the center of the protruding cylinder.

(4) As the angle of attack increases, the mass transfer peak on the base plate created by the counterrotating vortices diminishes, and almost disappears at $\alpha = 45$. On the other hand, the influence of the corner vortex on the mass transfer enhancement remains strong regardless of the angle of attack.

(5) Streaks of the corner vortex and the counterrotating vortices in the visualization pictures compare well with trails of the peak of mass transfer created by these vortices for all angles of attack.

REFERENCES

1. T. Igarashi, Characteristics of the flow around a square prism, *Bull. JSME* **27**, 1858–1865 (1984).
2. T. Igarashi, Heat transfer from a square prism to an air stream, *Int. J. Heat Mass Transfer* **28**, 175–181 (1985).
3. T. Igarashi, Local heat transfer from a square prism to an air stream, *Int. J. Heat Mass Transfer* **29**, 777–784 (1986).
4. R. J. Goldstein, S. Y. Yoo and M. K. Chung, Convective mass transfer from a square cylinder and its base plate, *Int. J. Heat Mass Transfer* **33**, 9–18 (1990).
5. S. Y. Yoo, A study on the mass transfer from a square cylinder and its base plate using naphthalene sublimation technique, Ph.D. Thesis, Korea Advanced institute of Science and Technology, Seoul, Korea (1989).
6. D. Ambrose, I. J. Lawrenson and C. H. S. Sparke, The vapor pressure of naphthalene, *J. Chem. Thermodyn.* **7**, 1173–1176 (1975).
7. N. H. Chen and D. F. Othmer, New generalized equation for gas diffusion coefficient, *J. Chem. Engng Data* **7**, 37–41 (1962).
8. P. H. Chen, Measurement of local mass transfer from a gas turbine blade, Ph.D. Thesis, University of Minnesota, Minneapolis, Minnesota (1988).
9. S. J. Kline and F. A. McClintock, Describing uncertainty in single-sample experiments, *Mech. Engng* **75**, 3–8 (1953).
10. T. Ota and H. Nishiyama, A correlation of maximum turbulent heat transfer coefficient in reattachment flow region, *Int. J. Heat Mass Transfer* **30**, 1193–1200 (1987).
11. E. M. Sparrow, S. S. Kang and W. Chuck, Relation between the points of flow reattachment and maximum heat transfer for regions of flow separation, *Int. J. Heat Mass Transfer* **30**, 1237–1246 (1987).
12. R. L. Simpson and R. L. Field, A note on the turbulent Schmidt and Lewis numbers in a boundary layer, *Int. J. Heat Mass Transfer* **15**, 177–180 (1972).
13. R. M. Kendall, Interaction of mass and momentum transfer in the turbulent boundary layer, Sc.D. Thesis, Massachusetts Institute of Technology, Cambridge, Massachusetts (1959).
14. S. M. You, T. W. Simon and J. Kim, Free-stream turbulence effects on convexly curved turbulent boundary layer, Trans. ASME, 86-WA/HT-46 (1986).
15. R. Hilpert, Wärmeabgabe von geheizten drähten und rohrem im luftstorm, *Gebiete Ingenieurw* **4**, 215–224 (1933).

16. P. A. Eibeck and J. K. Eaton, Heat transfer effects of a longitudinal vortex embedded in a turbulent boundary layer, *J. Heat Transfer* **109,** 16–24 (1987).
17. R. J. Goldstein, M. K. Chyu and R. C. Hain, Measurement of local mass transfer on a surface in the region of the base of a protruding cylinder with a computer controlled data acquisition system, *Int. J. Heat Mass Transfer* **28,** 977–985 (1985).
18. E. M. Sparrow, T. J. Stahl and P. Traub, Heat transfer adjacent to the attached end of a cylinder in crossflow, *Int. J. Heat Mass Transfer* **27,** 233–242 (1984).